Characterization of the mid-IR image quality at Gemini South

Dan Li, Charles M. Telesco, and Frank Varosi

Department of Astronomy, University of Florida, 311 Bryant Space Science Center, P.O.Box 112055, Gainesville, FL 32611, USA

ABSTRACT

To help the prospective observer take full advantage of the mid-IR capability of Gemini South, we characterize a key aspect of the mid-IR performance of the 8-meter telescope at Gemini-S, namely, the appearance and stability of its delivered mid-IR image profiles, with the goal of demonstrating that it can be used with a level of precision not used before. About 2000 images obtained with T-ReCS (a facility mid-IR camera at Gemini-S) between late 2003 and early 2009 were used for our image quality analysis. All targets are flux standards and recorded at one or more of the four bands Si-2 (8.74 μm), N (10.36 μm), Si-5 (11.66 μm), and Qa (18.3 μm). A non-linear least squares fitting of three profile models (Lorentzian, Gaussian, and Moffat) was performed on each image, and key parameters such as FWHM, ellipticity, position angle and Strehl-ratio were measured from the fitted profile. We find that the long-time-scale image quality is quite stable in terms of profile width or ellipticity, though short-time-scale variation is evident. We also examined the correlation between image quality and many ambient parameters and confirmed the interdependence between the image quality in the Qa band and the ambient humidity. The ellipticity of the profile was analyzed statistically as well. The average profiles for different filters can be used as important references in the future when a high-quality profile reference is not available during an observation.

Keywords: Mid-infrared, image quality, T-ReCS, Gemini-South

1. INTRODUCTION

The naturally better seeing at longer wavelengths coupled with the use of active optics have enabled nearly diffraction-limited performance in the mid-IR (roughly 8-25 μm) much of the time at major observatories like Gemini. However, most research has been done at lower angular resolution to avoid the challenge of working at the design limit of the telescope. For prospective observers to take full advantage of that hard-won, expensive capability at Gemini, a better understanding of the image quality, particularly the point-spread function (PSF), is required. To explore how far the facility's capabilities can be pushed, we carried out this Gemini PSF project to characterize a key aspect of the mid-IR performance of the Gemini South 8-meter telescope, namely, the appearance and stability of its delivered mid-IR image profiles, and tried to determine if it can be used with a level of precision not used before. This study provides the basis to realistically assess how well one can detect and characterize structures of astrophysical significance located close to bright sources in mid-IR images.

To illustrate some of the science motivation for this work, consider the following. Currently there are intense programs of mid-IR imaging and spectroscopy of planetary and protoplanetary disks around nearby ($<$200 pc) intermediate-mass, pre-main-sequence stars (i.e., Herbig Ae/Be stars) and young ($<$300 Myr) main-sequence stars being carried out by many research groups, including our group at the University of Florida. Results from our program include the co-discovery of the now well-known HR 4796A disk,[1,2] the first-ever detection and identification of silicates in circumstellar disks,[3,4] and acquisition of the evidence of a catastrophic collision of a large planetesimal in a young planetary disk.[5] Those objects are all highly extended (compared to the point source PSF), and therefore did not require working extremely close to the diffraction limit. However, in recently we needed to observe disks that are much smaller than those in the previous discoveries, which required us to more fully explore the facility's capabilities.

Further author information: (Send correspondence to Dan Li)
E-mail: dli@astro.ufl.edu, Telephone: 1 352 392 2052

The first example of those demanding observations is ζ *Lep*, a 230 Myr-old star with a dust disk resolved by T-ReCS,[6] the facility mid-IR camera at Gemini South. The disk is only 3 AU in radius, which is comparable to the size of Solar System's asteroid belt.[7] This discovery is important because the source may be the archetype for a whole new class of source: the asteroid-belt analogs. It also helps place our Solar System into the broader context of possible planetary-system configurations. However, in Fig. 1 we see that the emitting region of ζ *Lep* is just barely resolved, which means reliable information about the mid-IR PSF is crucial in order to derive key conclusions about the disk size.
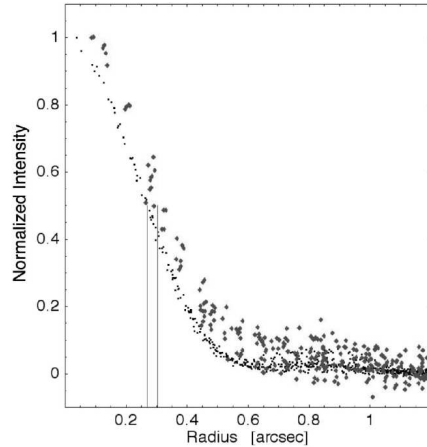

Figure 1. Azimuthally averaged intensity profiles at 18.3 μm of ζ Lep (diamonds) and reference PSF star (dots). The FWHM difference between the two profiles is indicated by the two vertical lines. The intrinsic half-width of the deconvolved disk is 0.14" $\pm$ 0.02", or 3.0 $\pm$ 0.4 AU.[7]

Another example is *AB Aur*, the archetype Herbig Ae/Be star, resolved with MICHELLE at Gemini North on two spatial scales: bright, very compact emission with a radius of about 10 AU, and fainter emission in the profile wings extending out to 350 AU (Fig. 2). Mariñas et al. (2006) showed that the compact structure is a combination of the unresolved hot inner rim of the central hole in an optically thick disk and the disk near 10 AU where it emerges from the shadow of the puffed-up rim. The more extended emission is the warm dust on the surface layer of the outer part of the optically thick flared disk.[8] In Fig. 2 we see that the detection of this extended structure relied on a careful subtraction of the PSF reference from the original image.

2. DATA AND REDUCTION

2.1 Data

We considered more than 1900 PSF images (Table 1) obtained with T-ReCS from late 2003 to early 2009. The targets were originally selected as mid-IR flux standards published by the MIRAC[9] and TIMMI-2[10] teams. Most stars are sufficiently bright to be detected with high S/N in all filters.[11] For a typical observation night, at least one set of such calibration-star images was taken at the beginning (before the observation of the science source), and several additional sets were taken throughout the night. From the figures shown in the following sections, we see that the data are almost evenly distributed through each year. Four different filters were used to obtain the calibration star images: Si-2, N, Si-5 and Qa, covering a wavelength range from 8 μm to 18 μm (Table 1). Among these four filters, N is a broad-band filter, and the other three are all narrow-band filters.

2.2 Reduction

i) Saveset stacking
In order to minimize the strong mid-IR background from the sky and telescope, all T-ReCS images are obtained in the so-called chop-nod mode, in which the telescope secondary mirror oscillates ("chops") at several hertz and the whole telescope moves back and forth ("nods") between two sky positions every 45 seconds or so (see
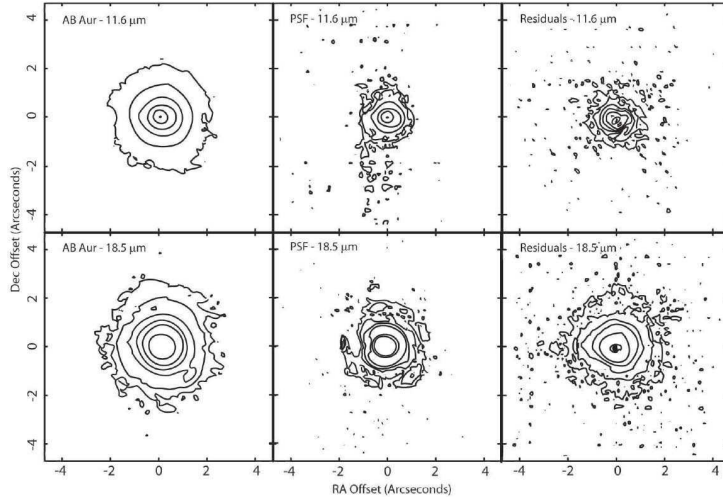
Figure 2. Mid-IR images of *AB Aur*. The reduced images, PSF references, and residuals (images with PSF subtracted) are shown in the left, middle and right panels, respectively. Residuals indicate that substantial resolved structure is seen in the wings of *AB Aur* profiles.[8]

Gemini mid-IR resource website for further information about this). As a result of this complex data-acquisition procedure, in each raw T-ReCS FITS file there are multiple extensions (all constituting a "saveset") corresponding to the images acquired at different chopping and nodding positions. In the first step of reduction, the multiple extensions in each FITS file are combined using $IRAF$ to form a single image of the target. Sometimes the raw FITS file may contain errors (e.g., one or more chopping sets are missing or improperly recorded), and so all images are visually inspected, and those with anomalies are eliminated from the image database before further reduction.

ii) PSF fitting

Next, we perform a non-linear least-squares fitting of three PSF models (Lorentzian, Gaussian, and Moffat) to every image. For each image, the fitting is executed many times at different orientations (every 5 degrees) relative to the PSF center, and by this means the 2-dimensional shape of the PSF can be determined. The morphological parameters such as the full-width at half-maximum (FWHM), the ellipticity, and the position angle (PA) can be measured as well.

iii) Strehl ratio

The strehl ratio (SR) is another frequently used indicator of image quality. It is defined as the ratio of the irradiance at the peak of an aberrated PSF to the irradiance obtained with a perfect (diffraction-limited) imaging system. We constructed a model of the Gemini exit pupil (a circular aperture with a central obscuration), from

Table 1. Number of images for PSF analysis.

Filter	λ (μm)	λ range (50% transmission, μm)	Number of images
Si-2	8.74	8.35 - 9.13	176
N (broad band)	10.36	7.70 - 12.97	1342
Si-5	11.66	11.09 - 12.22	169
Qa	18.3	17.57 - 19.08	241

which the theoretical PSF could be computed by means of Fast Fourier Transform (FFT), with the SR being derived from a comparison between the theoretical and observed PSFs. We note that the model of exit pupil we adopted was a rough approximation of the real exit pupil. In practice the computation of SR is tricky, with different methods sometimes leading to different results.[12] Therefore, we did not use the SR as an evaluation of the optical performance of the Gemini+T-ReCS system, but only as a measure of image quality for comparisons among the images within our database.

3. RESULTS AND DISCUSSION

3.1 Strehl Ratio

Figure 3 shows the SR distributions of all images. Generally there is a trend that as wavelength increases SR also increases, which is consistent with our knowledge regarding the image quality of a non-AO system. First, the coherence length of the atmospheric turbulence is larger when the wavelength is longer. Second, the imaging system becomes less sensitive to the aberrations caused by optical imperfection at longer wavelengths. If we apply the value SR=0.8 as a threshold of diffraction-limited image quality (i.e., the Marechal criterion), we can see that the image quality of the Qa images is close to the diffraction limit (about 50% of images have SR>0.55).

The temporal fluctuations of the SR are shown in Fig. 4. There seems to be no long-time-scale drift, but short-time-scale variances are obvious, especially for Si-5 images. For N images, the dispersion was smaller at the beginning of 2006, and has been relatively stable since then. For Qa images, the SR dispersion was smallest in 2006, and grew larger in the following two years; the mean value (not shown in the plot) also dropped slightly in 2007 and 2008, which may indicate a small decrease in the image quality.
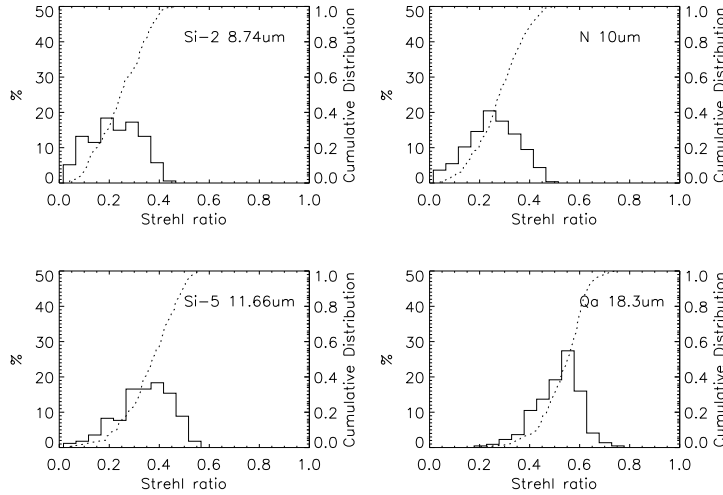

Figure 3. Strehl ratio distributions. Dotted lines are the cumulative distributions. For N filter, data obtained before 2006 are not included.

3.2 FWHM

The temporal variation of FWHM is shown in Fig. 5. The horizontal dashed lines represent the diffraction-limited FWHMs, which have a linear relation with the wavelength:

$$FWHM = 0.97\frac{\lambda}{D} \qquad (1)$$

The coefficient 0.97, which is smaller compared to the commonly used value, is due to the central obscuration of the telescope. Again, we see that the image quality does not change much over time, and that, as expected, the Qa band seems to have the most stable performance among all filters. Compared with Fig. 4, the data
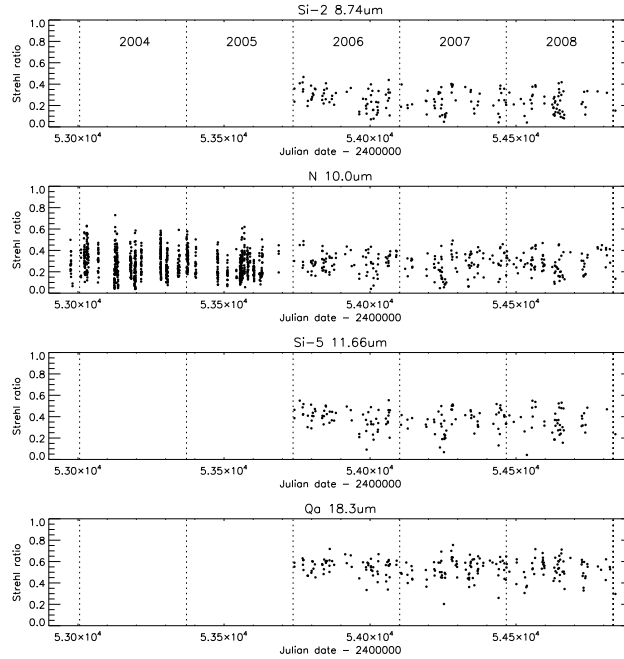
Figure 4. Strehl ratio vs. Julian date. Vertical dashed lines represent the beginning of each calendar year.
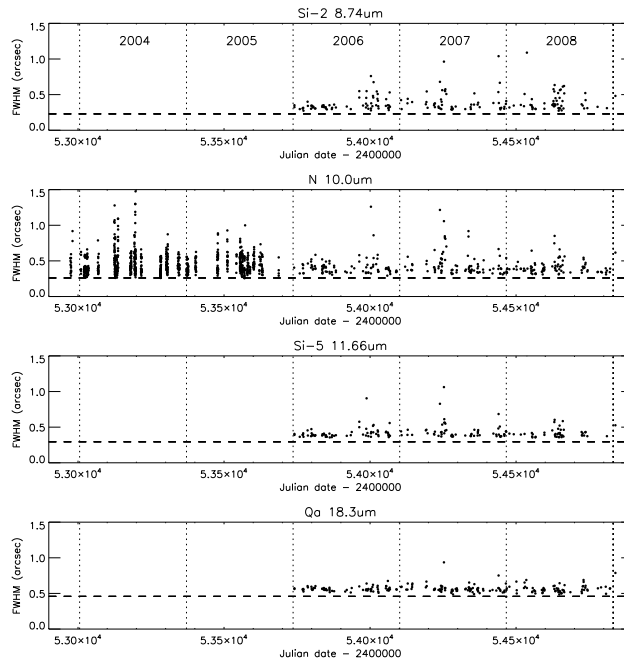

Figure 5. FWHM vs. Julian date. Horizontal dashed lines represent the diffraction-limited FWHM.

dispersion in Fig. 5 is obviously smaller. This difference suggests to us that the SR is a more sensitive measure of the image quality than FWHM when one is nearly diffraction-limited, as a direct comparison between them also indicates (Fig. 6).The overall trend between SR and FWHM is clear: a smaller FWHM means a higher SR. Furthermore, when the FWHM is getting close to the diffraction-limited value, the trend becomes much steeper, with a small change in FWHM leading to a large change in SR. In other words, the FWHM does not change as

noticeably as the SR does when the image quality is approaching the theoretical limit.
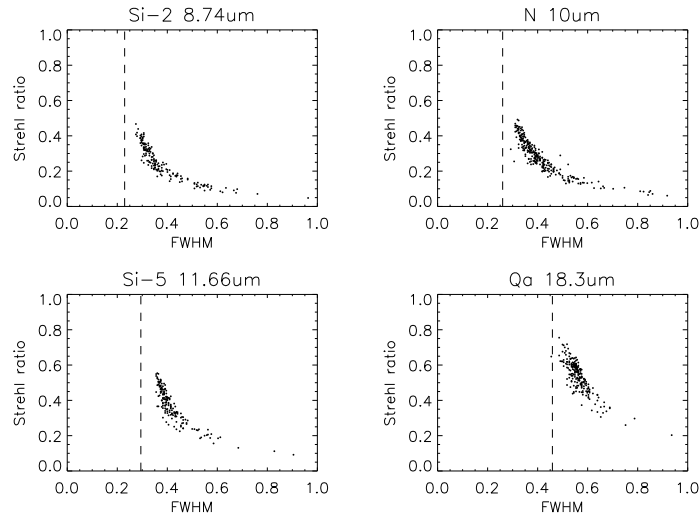

Figure 6. Comparison between SR and FWHM. Dashed lines are the diffraction-limited FWHM

3.3 The effect of humidity on the image quality

We notice that the short time-scale variations are quite obvious in Fig. 4. To explain this, we examine a number of parameters found in the FITS headers, including the observation date and local time, airmass, ambient temperature, humidity, and detector temperature, to see if any of them correlates with the large dispersion in the image quality measurements. However, no obvious correlation is found between those parameters and FWHM or SR, with only one exception in the Qa images where we see a weak correlation between humidity and SR (Fig. 7). This suggestion that the image quality in Qa band is more sensitive to the high humidity than other filters is consistent with the fact that there is strong water absorption within the Qa passband. Since the humidity is a local effect, it may be related in a complex way to ground-layer turbulence or other factors beyond the scope of the current study.
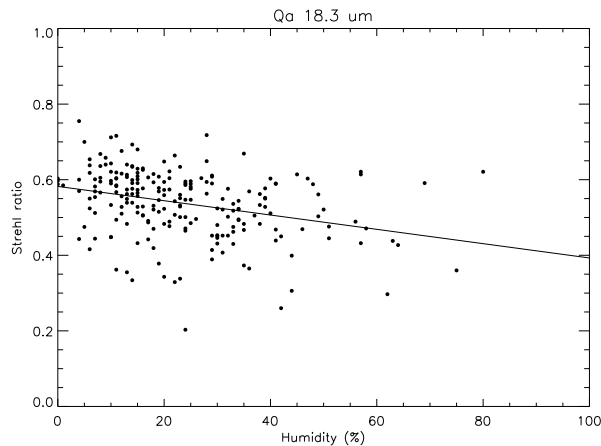

Figure 7. A weak correlation between ambient humidity and image quality (in terms of SR) observed in Qa images. Solid line is the linear fit of data.

3.4 Ellipticity

Ellipticity is defined as:

$$Ellipticity = \frac{(a - b)}{a} \qquad (2)$$

where a (semimajor axis) and b (semiminor axis) are both measured from the fitted PSF. This parameter is not only helpful in discriminating between point sources and those with physical extensions (e.g. circumstellar disks), but also a good indicator of image quality. To illustrate that, we make a comparison between ellipticity and SR, which is another measure of image quality, and find that there is indeed a correlation between them, especially for Si-5 and Qa images (left panel in Fig. 8). This information is very useful when we have an image with a small, but non-zero ellipticity (i.e., 0.1-0.2) and we want to know if it is intrinsic to the astronomical source, or just due to optical imperfections. Referring to the correlations in Fig. 8, if the image has a high SR (i.e., $SR \geq 0.4$ for Si-2, N and Si-5 images, $SR \geq 0.5$ for Qa images), there is a higher probability that the elliptical PSF reflects the real physical extension of the object. On the other hand, if the SR is low, it is likely that the high ellipticity is caused by something else.
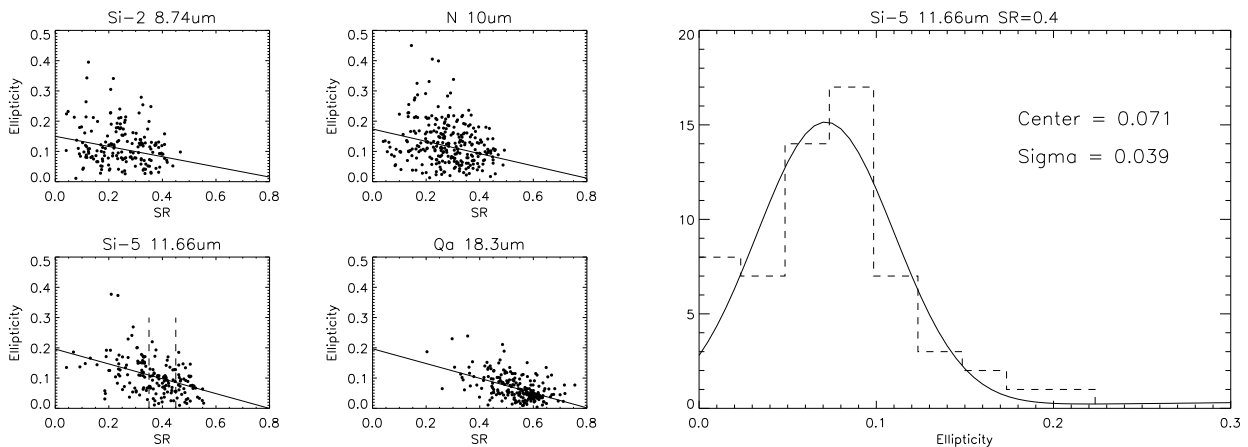

Figure 8. Left panel: correlation between ellipticity and SR. Solid lines are the linear fits. Data between the two dashed lines in the Si-5 plot are used to construct the ellipticity histogram in the right panel.

To make better use of the information provided by ellipticity and SR, we can construct a series of standard ellipticities based on the delivered images. For example, if we look at images with a small range of SR (e.g. Si-5 images with 0.35<SR<0.45, as shown in Fig. 8), and plot their ellipticity histogram (right panel in Fig. 8), we can see that the data fit a Gaussian profile very well. Assume that we have a new image with SR falling in this range, and the measured ellipticity is 0.2, which is, according to Fig. 8, barely outside 3σ. In this case we can say that this ellipticity is probably due to the physical elongation of the source rather than the aberrations of the instruments, since we seldom see an image with a similar SR also having such a high ellipticity in our database of calibration stars. Similarly, the standard ellipticities corresponding to other filters and SR ranges can be computed, as summarized in Table 2.

Nevertheless, we want to stress that the observer should always be cautious with the ellipticity measurement or any morphology-related studies with mid-IR images. Our analysis shows that even a large non-zero ellipticity can be produced by instrumental, seeing, or other effects. Obviously, a more careful treatment is necessary for any analysis that relies on the source morphology or angular-size measurement. One example of such higher-precision measurements can be found in the work of Mariñas et al. (2006), where the raw mid-IR file was split into a series of savesets to minimize the seeing and chopping effects on the FWHM measurements.[8]

3.5 Averaged PSF

The PSF profiles (Gaussian and Moffat) averaged over all available images are shown in Fig. 9 and 10. We do not include the averaged Lorentzian profiles for two reasons. First, to describe a Lorentzian profile we need

Table 2. Ellipticity distributions in different Strehl ratio range.

Filter	SR range	Center	δ
Si-2	0.35 - 0.45	0.057	0.064
	0.25 - 0.35	0.061	0.086
	0.15 - 0.25	0.072	0.084
	0.05 - 0.15	0.080	0.030
N	0.35 - 0.45	0.080	0.056
	0.25 - 0.35	0.088	0.081
	0.15 - 0.25	0.111	0.082
	0.05 - 0.15	0.089	0.020
Si-5	0.45 - 0.55	0.051	0.050
	0.35 - 0.45	0.071	0.039
	0.25 - 0.35	0.099	0.068
	0.15 - 0.25	0.114	0.046
Qa	0.55 - 0.65	0.028	0.017
	0.45 - 0.55	0.056	0.044
	0.35 - 0.45	0.083	0.046

at least three parameters (radius at half maximum, power scaling from the center and power exponent factor), each of which contributes to the profile in a different way, which makes it tricky to define an *averaged* Lorentzian profile. Second, a Lorentzian profile is similar to a Gaussian in the central part of the PSF, and their FWHM values are approximately the same. The FWHM of the averaged Gaussian profiles are shown in the figure. For Moffat profiles, the FWHM can be calculated by the formula:

$$FWHM = 2\alpha\sqrt{2^{1/\beta} - 1} \tag{3}$$

where α and β are shown in Fig. 10 (α is in the unit of arcsec, and β is dimensionless). Observers can use those averaged Gaussian/Moffat profiles shown in Fig. 9 and 10 as empirical references if there is no high-quality PSF reference star available during an observation. These average profiles also give us a general idea of the actual resolution that Gemini South and T-ReCS can achieve routinely.

4. SUMMARY

The goal of the Gemini PSF project has been to characterize the mid-IR image quality at Gemini South, in terms of the PSF appearance and stability, and by doing so to provide observers with reliable and basic knowledge of the mid-IR capability currently achievable at that facility. We have used about 1900 images of flux calibration stars to carry out our PSF analysis. All of these data were obtained with T-ReCS, the facility mid-IR camera at Gemini South, and they cover a wide wavelength range (from 8.7 μm to 18.3 μm) and a long time interval (from late 2003 to early 2009). Our statistical analysis of these data lead us to the following conclusions:

1) In terms of PSF size and Strehl ratio, the image quality of Gemini South with T-ReCS has been quite stable since 2006;

2) Strehl ratio is a better measure of image quality than is FWHM, especially when the image quality is close to the diffraction limit;

3) The ambient humidity is weakly, but noticeably, correlated with the quality of the Qa (18.3 μm) images;

4) There is a statistical correlation between the SR and the ellipticity of the image profile, and observers should be cautious with non-zero ellipticities measured from the mid-IR images;

5) The average PSF profiles, which can be used as artificial references for future observations, are computed for four filters and two PSF models.
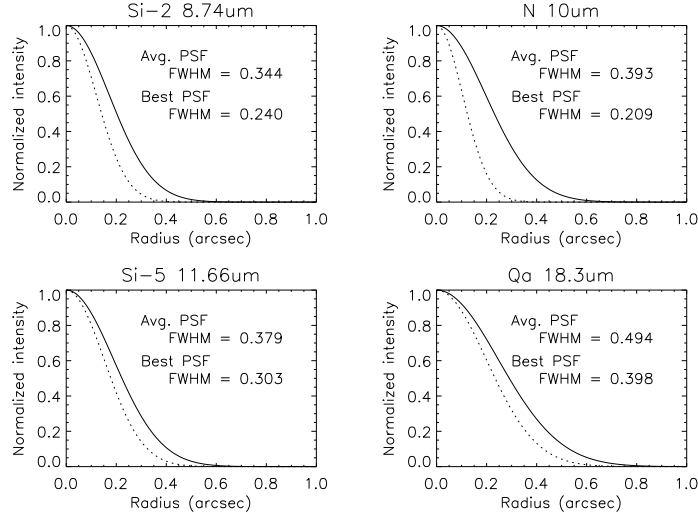
Figure 9. Averaged Gaussian profiles (solid lines). The dotted lines show the best PSFs (with the smallest FWHMs) in the database.
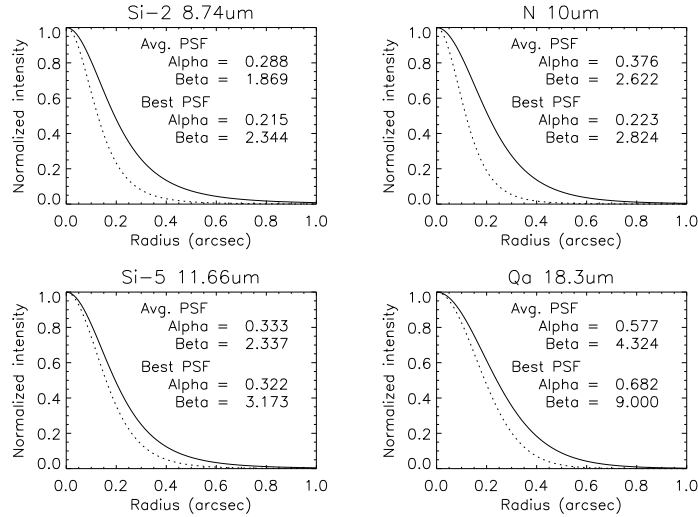

Figure 10. Averaged Moffat profiles (solid lines). The dotted lines show the best PSFs (with the smallest FWHMs) in the database.

Working close to the diffraction limit of a telescope is a delicate and risky procedure, but one that is essential in order to push the science envelope explored by a frontline facility as important as Gemini. We believe that the results we have obtained provide the most comprehensive and detailed information on the mid-IR image quality of Gemini South, and will make it a more powerful and competitive observatory.

ACKNOWLEDGMENTS

REFERENCES

[1] Jayawardhana, R., Fisher, R. S., Hartmann, L., Telesco, C., Pina, R., and Fazio, G., "A dust disk surrounding the young A star HR 4796A," *ApJL* **503**, 79 (1998).

[2] Telesco, C. M., Fisher, R. S., Pina, R. P., Knacke, R. F., Dermott, S. F., Wyatt, M. C., Grogan, K., Holmes, E. K., Ghez, A. M., Prato, L., Hartmann, L. W., and Jayawardhana, R., "Deep 10 and 18 micron imaging of the HR 4796A circumstellar disk: Transient dust particles and tentative evidence for a brightness asymmetry," *ApJ* **530**, 329–341 (2000).

[3] Telesco, C. M. and Knacke, R. F., "Detection of silicates in the Beta Pictoris disk," *ApJL* **372**, 29–31 (1991).

[4] Knacke, R. F., Fajardo-Acosta, S. B., Telesco, C. M., Hackwell, J. A., Lynch, D. K., and Russell, R. W., "The sillicates in the disk of Beta Pictoris," *ApJ* **418**, 440 (1993).

[5] Telesco, C. M., Fisher, R. S., Wyatt, M. C., Dermott, S. F., Thomas, T. J. J., Novotny, S., Marinas, N., Radomski, J. T., Packham, C., Buizer, J. D., and Hayward, T. L., "Mid-infrared images of Beta Pictoris and the possible role of planetesimal collisions in the central disk," *Nature* **433**(7022), 133–136 (2005).

[6] Telesco, C. M., Pina, R. K., Hanna, K. T., Julian, J. A., Hon, D. B., and Kisko, T. M., "GatirCam: Gemini mid-infrared imager," in [*Infrared Astronomical Instrumentation*], Fowler, A. M., ed., *Proc. SPIE* **3354**, 534–544 (1998).

[7] Moerchen, M. M., Telesco, C. M., Packham, C., and Kehoe, T. J. J., "Mid-infrared resolution of a 3 AU radius debris disk around ζ Leporis," *ApJ* **655**, 109–112 (2007).

[8] Marinas, N., Telesco, C. M., Fisher, R. S., Packham, C., and Radomski, J. T., "Mid-infrared imaging of the Herbig Ae star AB Aurigae: extended emission on several scales," *ApJ* **653**, 1353–1357 (2006).

[9] Hoffmann, W. F., ad K. Shivanandan, G. G. F., Hora, J. L., and Deutsch, L. K., "MIRAC: a mid-infrared array camera for astronomy," in [*Infrared Detectors and Instrumentation*], Fowler, A. M., ed., *Proc. SPIE* **1946**, 449–460 (1993).

[10] Reimann, H., Weinert, U., and Wagner, S., "TIMMI 2: a new MIR multimode instrument for ESO," in [*Infrared Astronomical Instrumentation*], Fowler, A. M., ed., *Proc. SPIE* **3354**, 865–876 (1998).

[11] Hayward, T. L., "An analysis of T-ReCS quality-assessment imaging, 2003-2006," *Private communication* (2006).

[12] Roberts, L. C. J., Perrin, M. D., Marchis, F., Sivaramakrishnan, A., Makidon, R. B., Christou, J. C., Macintosh, B. A., Poyneer, L. A., van Dam, M. A., and Troy, M., "Is that really your Strehl Ratio?," in [*Advancements in Adaptive Optics*], Calia, D. B., Ellerbroek, B. L., and Ragazzoni, R., eds., *Proc. SPIE* **5490**, 504–515 (2004).